



JOINT INSTITUTE FOR NUCLEAR RESEARCH

Dzelepov Laboratory of Nuclear Problems

**FINAL REPORT ON THE
SUMMER STUDENT PROGRAM**

**Optical simulation of the PMT quantum efficiency and
its impact to the JUNO detector resolution**

Supervisor:
Tatiana Antoshkina

Student:
Natalya Kovyazina, Russia
Irkutsk State University

Participation period:
July 30 – September 18

Dubna, 2018

Contents

Introduction	2
1 JUNO experiment	3
1.1 JUNO Detector	3
2 PMT	5
2.1 PMT mass-testing methods	5
2.1.1 Container approach	5
2.1.2 Scanning station	6
2.2 Optical processes	7
3 Modeling of optical processes inside the detector and PMT	10
4 Results	13
Conclusion	17
Bibliography	18

Introduction

In recent years more and more experiments aimed at studying neutrinos have appeared. Most of these experiments use neutrino detectors. Huge collaborations are engaged in the design, construction, testing and maintenance of the neutrino detectors. In this paper the JUNO project is considered, also simulated optical processes inside the detector and PMT.

Chapter 1

JUNO experiment

The Jiangmen Underground Neutrino Observatory (JUNO) is a multi-purpose neutrino experiment. The experiment locates in Jinji town, Kaiping city, Jiangmen city, Guangdong province. The experimental site is 43 km to the southwest of the Kaiping city, a county-level city in the prefecture-level city Jiangmen in Guangdong province. There are five big cities, Guangzhou, Hong Kong, Macau, Shenzhen, and Zhuhai, all in ~ 200 km drive distance, as shown in Figure 1.1. The experimental site is at ~ 53 km from the Yangjiang NPP and Taishan NPP. Yangjiang NPP has six reactor cores of 2.9 GW th each (thermal power). Taishan NPP has planned four cores of 4.59 GW th each.



Figure 1.1: The JUNO experiment location.

1.1 JUNO Detector

The JUNO detector consists of a central detector, a water Cherenkov detector and a muon tracker. The central detector is a liquid scintillator (LS) detec-

tor of 20 kton fiducial mass with an designed energy resolution of $3\%/E(\text{MeV})$. The central detector is submerged in a water pool to be shielded from natural radioactivity from the surrounding rock and air. The water pool is equipped with Photomultiplier Tubes (PMTs) to detect the Cherenkov light from cosmic muons, acting as a veto detector. On top of the water pool, there is another muon detector to accurately measure the muon tracks. A schematic view of the JUNO detector is shown in Figure 1.2.

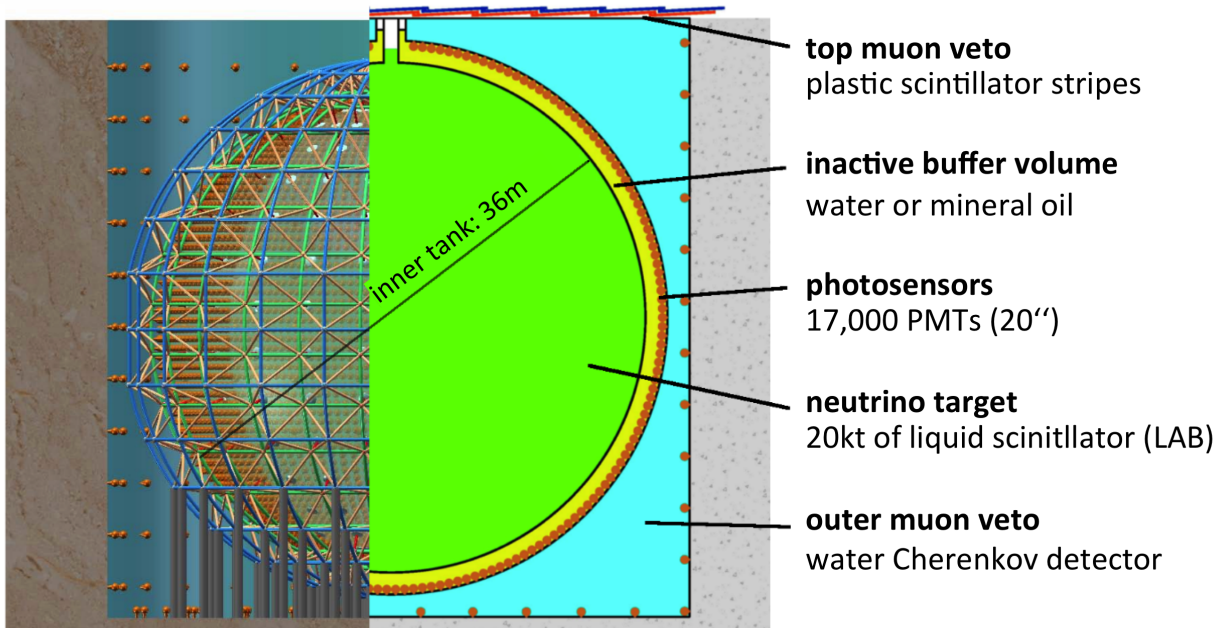


Figure 1.2: A schematic view of the JUNO detector.

The photoelectron yield has been tuned according to the Daya Bay data. To reach the required energy resolution, the following improvements from Daya Bay have to be accomplished.

- The PMT photocathode coverage $\geq 75\%$
- The PMT photocathode quantum efficiency $\geq 35\%$.
- The attenuation length of the liquid scintillator ≥ 20 m at 430 nm, which corresponds to an absorption length of 60 m with a Rayleigh scattering length of 30 m.

Chapter 2

PMT

Photomultiplier tubes (PMTs) are widely used in astrophysics, nuclear and particle physics. In many cases, the only optical property of a PMT of interest for the design of an experiment is its spectral sensitivity, i.e., the fraction of photons converted into detected photoelectrons as a function of the wavelength. Three processes are possible for a photon impinging on a PMT:

1. Absorption in the photocathode, with probability $A(\lambda, \theta)$
2. Reflection from the PMT window or photocathode, with probability $R(\lambda, \theta)$
3. Transmission through the photocathode inside the PMT, with probability $T(\lambda, \theta) = 1 - R(\lambda, \theta) - A(\lambda, \theta)$

In case of absorption, a photoelectron is produced, which has a certain probability to escape the layer towards the interior of the PMT, to be accelerated to the first dynode and start an avalanche, resulting in a detectable signal. It is convenient to express the probability that a photon contributes to a signal, so called quantum efficiency QE, as the product of two probabilities:

$$\text{QE} = A(\lambda, \theta) \times P_{\text{conv}}(\lambda)$$

where $A(\lambda, \theta)$ is the probability that the photon is absorbed in the photocathode, which is a function of the wavelength λ and the incidence angle θ and P_{conv} is the conversion factor for such absorption to result in an avalanche.

2.1 PMT mass-testing methods

2.1.1 Container approach

All of the 17739 large-photocathode 20-inch PMTs will be tested in 4 containers which are designed and produced by the team from the University of Hamburg and the University of Tübingen. Each container is a 20" refrigerated container that can control the temperature within a range between -20°C and

45°C with a precision of less than 1°C. In addition, the containers are lined with a multi-layer magnetic shielding based on silicon iron that guarantees a magnetic field of less than 10% of the EMF in each of the 36 measurement positions. To provide identical and reproducible measurement conditions each container is equipped with 36 precision-made drawer boxes housed in a shelf, as can be seen in Figure 2.1. The complete shelf system (including the boxes) is made from aluminum, and nearly all surfaces inside the container and the drawer boxes are black. The PMTs are placed on removable trays equipped with a precise holder made from anti-static foam. The trays are then fixed to the drawer by a clamping lever, allowing for the precise positioning of the PMTs inside each drawer.

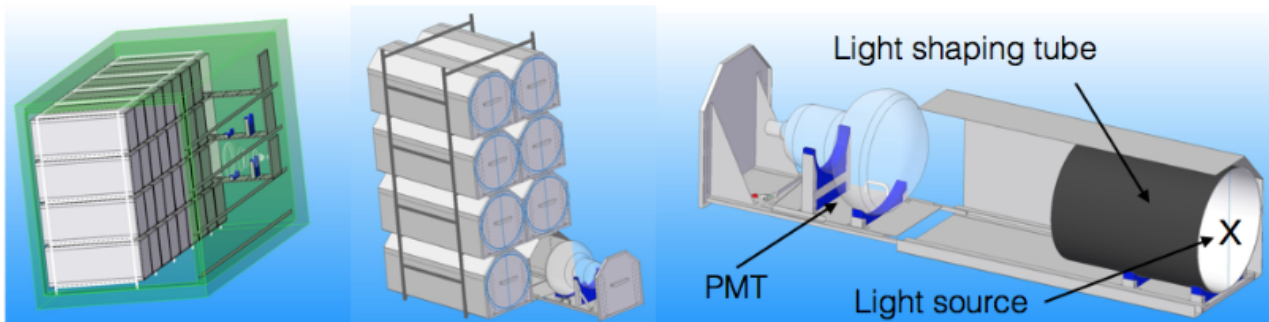


Figure 2.1: The Container: general view (left), drawers (middle), PMT layout in a drawer (right).

On the other side of the drawer boxes the light sources are mounted 50 cm away from the top of the PMT. The light sources are stabilized LEDs produced by the HVSYS company, and are also used in the scanning stations. They are deployed behind optics (including a diffuser) designed to generate a suitable light field to illuminate the entire surface of the 20" PMTs with an intensity between 0.1 and 1.5 photons per LED pulse. A large light shaping tube, coated black on one side and equipped with highly reflecting Tyvek on the other side, ensures that the sides of the PMTs are also illuminated (see Figure 2.1 right). In addition, two of the four containers will be equipped with a picosecond Laser (wavelength of about 420 nm). The light of the lasers will be distributed by optical fibers producing a light field of similar intensity but within a narrower cone. Not all of the PMT characteristics can be tested inside the container. The container will mainly test the PDE and TTS of the PMTs, as well as the dark count rate and the pre- and after-pulse rates.

2.1.2 Scanning station

The container approach is not sensitive to inhomogeneities of characteristics along the PMT's photocathode surface. Since all of the measurements in the container are performed in a constantly compensated magnetic field at the

level of a few μT , it does not allow for the testing of a PMT's magnetic field sensitivity. In order to obtain these measurements a sampling of about a thousand PMTs will be tested more precisely. A special setup, called the scanning station, was designed and produced at the Joint Institute for Nuclear Research (see Figure 2.2). The scanning station is placed in a light-tight dark room. In order to adjust/compensate for the EMF inside the black room Helmholtz coils are installed within the walls, floor and ceiling. The core of the scanning station is a rotating frame with 7 stabilized compact pulsed light generators that are placed at different zenith angles. The frame is rotated by a step motor and covers all 360° azimuthal angles. A support system that holds the PMT allows for rotations in different spatial positions in order to put the PMT into different orientations with respect to the magnetic field provided by the dark room. It allows for the testing of individual PMTs in all relevant aspects by scanning the photocathode, and allows for an in-depth understanding of the performance of a PMT, and may identify any potential problems.

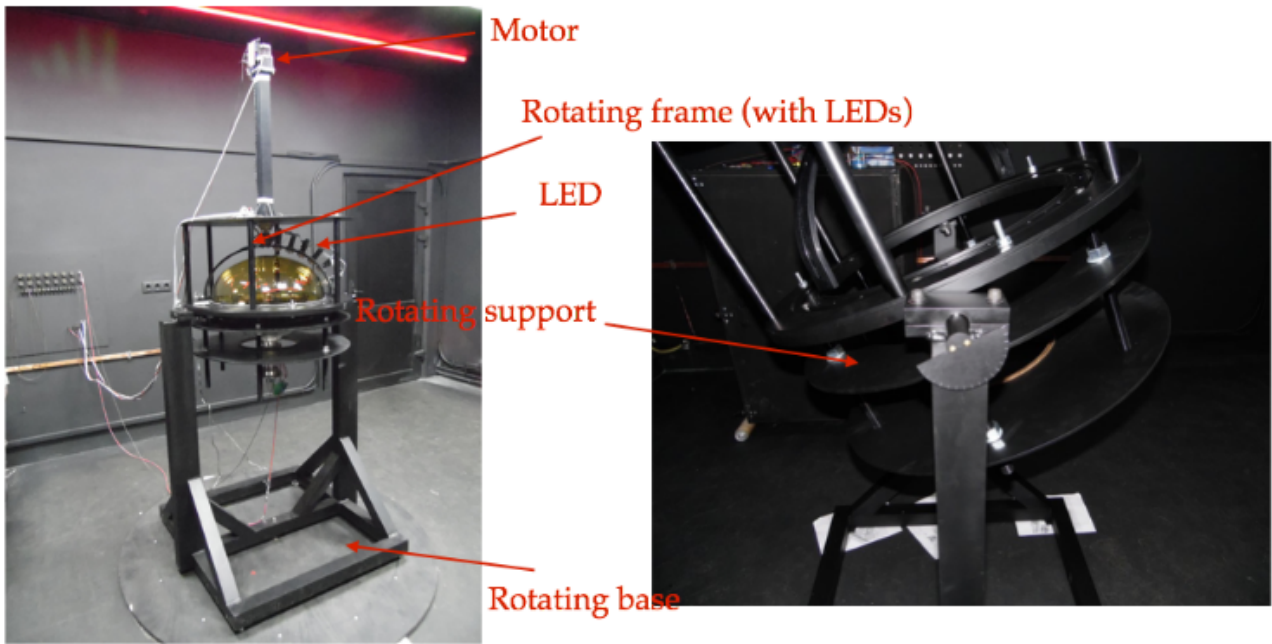


Figure 2.2: Scanning station general view in the dark room (left) and rotating support (right).

2.2 Optical processes

Dealing with light reflection from a PMT, four regions can be defined, each characterized by its own refractive index:

- The medium where the light originates, with n_1 ;
- The PMT glass envelope, with n_2 ;
- The photocathode, with $n_3 = n_{\text{ph}} + \imath k_{\text{ph}}$

- The vacuum inside the PMT, with n_4 .

The amplitudes of the reflected and transmitted waves at the interface glass-photocathode ($n_2 - n_3$) are given by the following formulas:

$$\begin{aligned} a_{\text{R}}(\lambda, \theta) &= r_{23} + \frac{t_{23}t_{32}r_{34} \exp(-2\imath\delta)}{1 + r_{23}r_{34} \exp(-2\imath\delta)} \\ a_{\text{T}}(\lambda, \theta) &= \frac{t_{23}r_{34} \exp(-\imath\delta)}{1 + r_{23}r_{34} \exp(-2\imath\delta)} \end{aligned} \quad (2.1)$$

where

$$\begin{aligned} r_{ij} &= \frac{n_i \cos \theta_{i(j)} - n_j \cos \theta_{j(i)}}{n_i \cos \theta_{i(j)} + n_j \cos \theta_{j(i)}} \\ t_{ij} &= \frac{2n_i \cos \theta_{i(j)}}{n_i \cos \theta_{i(j)} + n_j \cos \theta_{j(i)}} \\ \delta &= \frac{2\pi d n_3}{\lambda} \cos \theta_3 \end{aligned} \quad (2.2)$$

In previous equations n_l is the refractive index of the l -th region, θ_k is the angle of the propagating light beam with respect to the normal in the same region. This is calculated using Snell's law starting from the angle of incidence on the PMT window $\theta_k = \theta$. All functions and variables in this section equations are complex, and the imaginary part of n_1 , n_2 and n_4 is set to 0. Eq. (2.1) holds for both light polarizations, perpendicular and parallel relative to the photocathode plane (defined as s and p waves, respectively), provided that the definitions for r_{ij} and t_{ij} are changed by swapping the i and j indices as indicated in Eq. (2.2) (the formulas with first indices apply to the s-wave). Eq. (2.1) can be used to predict the total reflectance of the PMT by adding the Fresnel reflection at the medium-to-window interface (n_1-n_2) to the reflectance from the photocathode:

$$\begin{aligned} R_{\text{tot}} &= \frac{1}{2} [R_s^{\text{tot}}(\lambda, \theta) + R_p^{\text{tot}}(\lambda, \theta)] \\ R_{s,p}^{\text{tot}} &= F_{s,p} + \frac{R_{s,p}(1 - F_{s,p})^2}{1 - F_{s,p}R_{s,p}} \\ R_{s,p} &= |a_{\text{R}}^{s,p}|^2 \end{aligned} \quad (2.3)$$

where the quantities:

$$\begin{aligned} F_s(\lambda, \theta) &= \left[\frac{\sin(\theta_1 - \theta_2)}{\sin(\theta_1 + \theta_2)} \right]^2 \\ F_p(\lambda, \theta) &= \left[\frac{\tan(\theta_1 - \theta_2)}{\tan(\theta_1 + \theta_2)} \right]^2 \end{aligned} \quad (2.4)$$

represent the Fresnel reflection coefficients at the interface with the PMT window. Similarly for the transmittance:

$$\begin{aligned}
 T_{tot}(\lambda, \theta) &= \frac{1}{2} [T_s^{tot}(\lambda, \theta) + T_p^{tot}(\lambda, \theta)] \\
 T_{s,p}^{tot}(\lambda, \theta) &= \frac{T_{s,p}(1 - F_{s,p})}{1 - F_{s,p}R_{s,p}}
 \end{aligned}
 \tag{2.5}$$

$$T_{s,p}(\lambda, \theta) = \frac{n_4 \cos \theta_4}{n_2 \cos \theta_2} |a_T^{s,p}|^2
 \tag{2.6}$$

The last optical function, absorption, is deduced from Eqs. (2.3) and (2.5), by using the identity:

$$A(\lambda, \theta) = 1 - R(\lambda, \theta) - T(\lambda, \theta)
 \tag{2.7}$$

Chapter 3

Modeling of optical processes inside the detector and PMT

The main requirement for a photomultiplier is Photo Detection Efficiency (PDE). Theoretically, the average PDE from all points of the photomultiplier is given by:

$$\overline{\text{PDE}} = \iint \text{PDE}(\Omega, \alpha) \frac{d^2\Phi}{d\Omega d\alpha} d\Omega d\alpha = \iint A(\Omega, \alpha) P_{p.e.}(\Omega, \alpha) \frac{d^2\Phi}{d\Omega d\alpha} d\Omega d\alpha, \quad (3.1)$$

where $A(\Omega, \alpha)$ is a photocathode absorption coefficient and $P_{p.e.}(\Omega, \alpha)$ is a probability to produce a photo-electron.

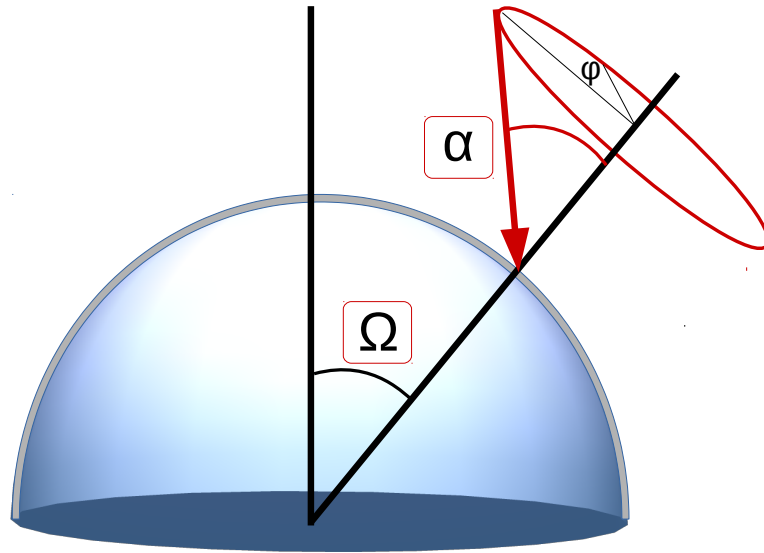


Figure 3.1: Definition of solid angles.

As the scanning station has 7 LEDs to test the PDE we can divide each photomultiplier into several "belts" (7 belts), each with its own PDE_i . It is taken into account that inside each belt the PDE should be constant, i.e. $\text{PDE}_i = \text{const.}$

Taking into account these data, 3 models will be considered in this paper:

1. $PDE_1 = PDE_2 = \dots = PDE_7$ - "constant" model
2. $PDE_{i+1} = PDE_i - \Delta PDE$ - "linear" model, ΔPDE - the step with which the PDE decreases. For simplicity, assume that $\Delta PDE = 1\%$
3. $PDE_{i+1} = PDE_i - \Delta PDE_i$ - "real" model, ΔPDE_i - step, changing PDE for each subsequent belt in table 3.1.

ΔPDE_1	ΔPDE_2	ΔPDE_3	ΔPDE_4	ΔPDE_5	ΔPDE_6
1.11%	1.08%	0.96%	-0.55%	0.39%	2.35%

Table 3.1: ΔPDE_i for "real" model.

When any photomultiplier is placed in a container, then some average PDE is measured. In this case, the internal structure of the PMT (different belts) is not taken into account. The average PDE is calculated in a very simple way

$$\overline{PDE} = \sum_i w_i PDE_i, \quad (3.2)$$

where w_i is the weight of each belt $i = 1, 2, \dots, 7$.

Weights can be calculated in two ways:

1. calculation of the contribution of each belt area to all PMT surface;
2. the same but taking into account the light field distribution inside the container.

When a large number of photomultipliers is tested in the container, their average PDE will form a Gaussian distribution that has an average μ and variance σ . For the initial simulation, it is necessary to collect 17739 PMTs, based on the actual distribution of the measured PDE, considering $\mu = 27\%$ and $\sigma = 3\%$. The strategy is as follows:

1. For each PMT, its average PDE is found from the Gaussian distribution with the parameters of the mean and variance (see Figure 3.2).
2. It is further determined whether this average PDE (\overline{PDE}) is greater or less than the manually set threshold PDE_{th} .

If the average PDE is greater ($\overline{PDE} \geq PDE_{th}$), the PMT is considered. If not, this photomultiplier is dropped out of consideration. At the same time, a counter is maintained, how many of the photomultipliers were examined and how many of them were taken.

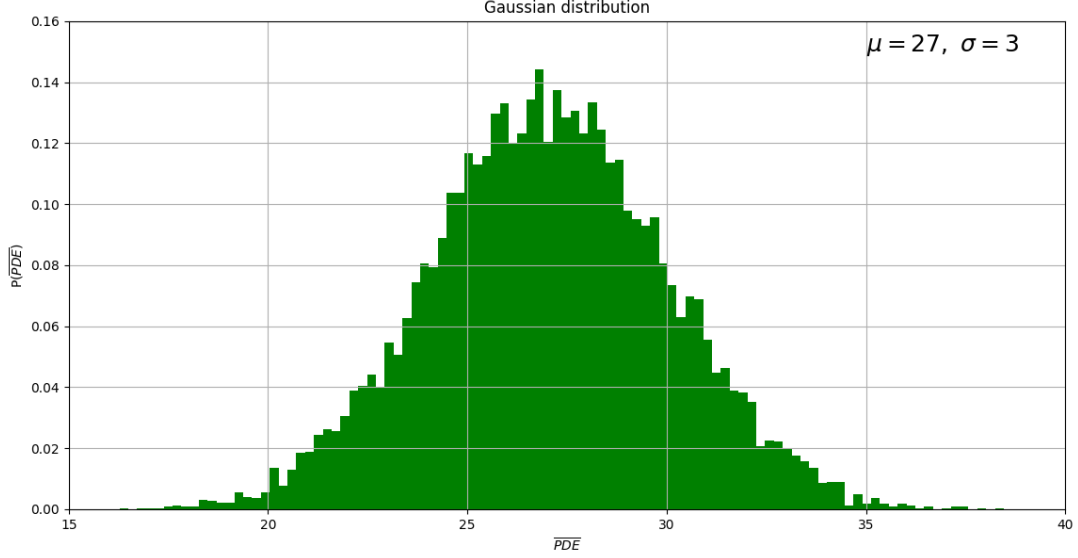


Figure 3.2: Gaussian distribution.

- Based on three earlier mentioned models of the PDE distribution belts ("constant", "linear" and "real"), the PDE map for the photomultiplier is filled, and then the data is saved for both types of each belt weights. In tables 3.2 and 3.3 these PDE maps are shown for one of the PMTs chosen from distribution with threshold of 29%.

	PDE ₁	PDE ₂	PDE ₃	PDE ₄	PDE ₅	PDE ₆	PDE ₇
sq	36.20%	35.20%	34.20%	33.20%	32.20%	31.20%	30.20%
sq+lf	35.28%	34.28%	33.28%	32.28%	31.28%	30.28%	29.28%

Table 3.2: Model "Linear" for threshold 29%

	PDE ₁	PDE ₂	PDE ₃	PDE ₄	PDE ₅	PDE ₆	PDE ₇
sq	33.39%	32.28%	31.20%	30.24%	30.79%	30.40%	28.05%
sq+lf	33.77%	32.66%	31.58%	30.62%	31.17%	30.78%	28.43%

Table 3.3: Model "Real" for threshold 29%

- The actions are repeated until 17739 PMTs are collected. If the counter of the total number of photomultipliers considered exceeds 100000, then the process must be stopped and another model of belts or another threshold should be considered.
- Then all these collected PMTs should be placed into the JUNO detector simulation in order to collect simulated light from IBD events and to convert it into the electrons, which create a signal we can detect. The mean number of electrons give as the opportunity to calculate the detector resolution as a function of the distance from the detector's center.

Chapter 4

Results

We considered 3 models - "Constant", "Linear" and "Real" - of PDE distribution and several thresholds as a testing criteria to collect required amount of PMTs. The results of our calculations for various thresholds (20%, 24%, 29%) for these three models are presented on the Figures 4.1 - 4.3).

First we took the threshold of 20%. It means that the greatest part of the PMTs from Gaussian distribution (see Figure 3.2) can be accepted in the testing process. The detector resolution as $1/\sqrt{\mu}$, where μ is the mean number of photo-electrons, is presented on Figure 4.1 as a function of the distance from the center of detector to the event point. The left plot corresponds to belt weights calculated only from the area each belt occupies. The right plot corresponds to calculated belt weights taking into account also the light field distribution inside the container.

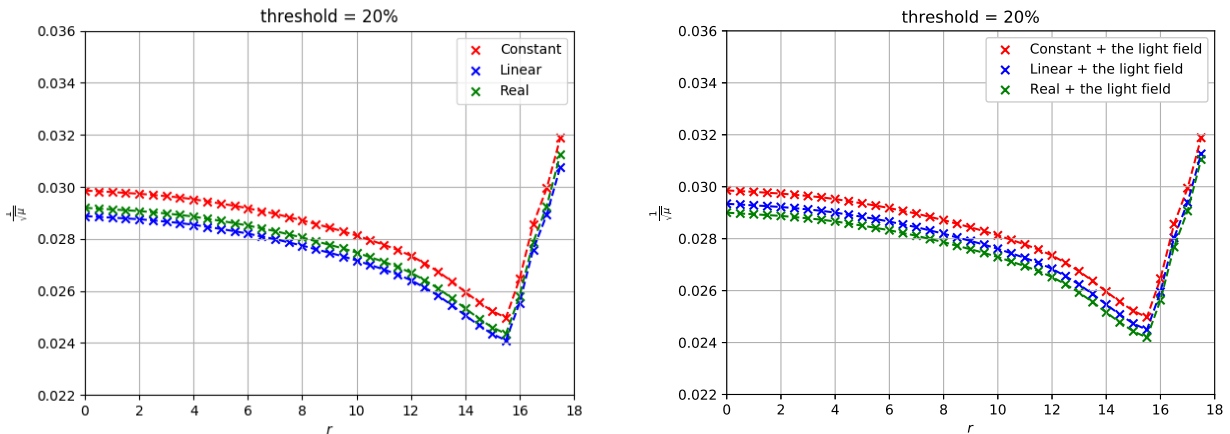


Figure 4.1: Detector energy resolution as a function of the distance from the center of detector to the event point with testing threshold $PDE_{th} = 20\%$.

Second we took the threshold of 24% - the threshold that now is taken in JUNO container testing process. The same plots for detector energy resolution as a function of the distance from the center of detector to the event point are shown on Figure 4.2.

And finally we took the threshold of 29%. It means that great part of the PMTs from Gaussian distribution (see Figure 3.2) aren't accepted in the testing

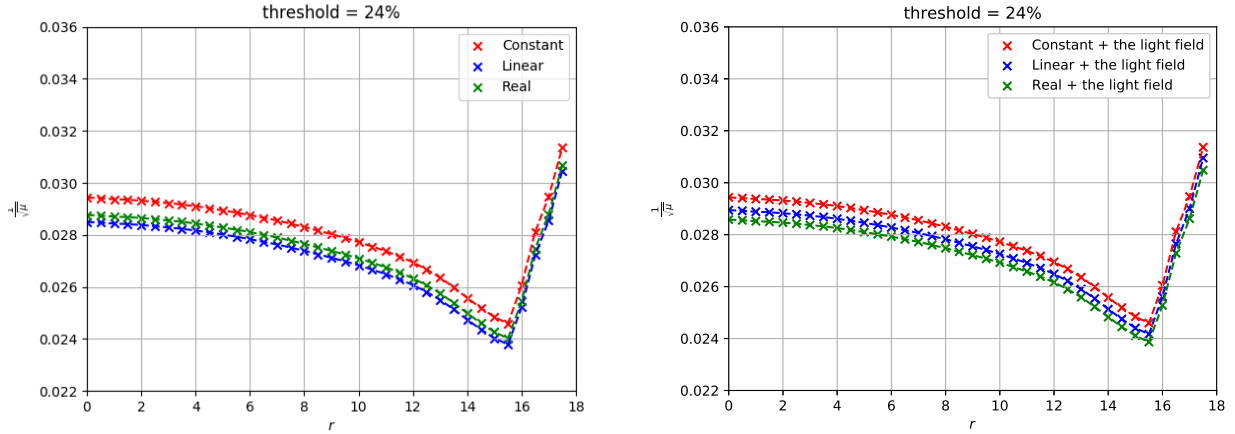


Figure 4.2: Detector energy resolution as a function of the distance from the center of detector to the event point with testing threshold $PDE_{th} = 24\%$.

process because their average PDE is less than threshold $\overline{PDE} < PDE_{th}$. It's the last threshold (with 1% difference) which allow us to collect 17739 PMTs by testing less than 100000 of them. The result you can see on Figure 4.3.

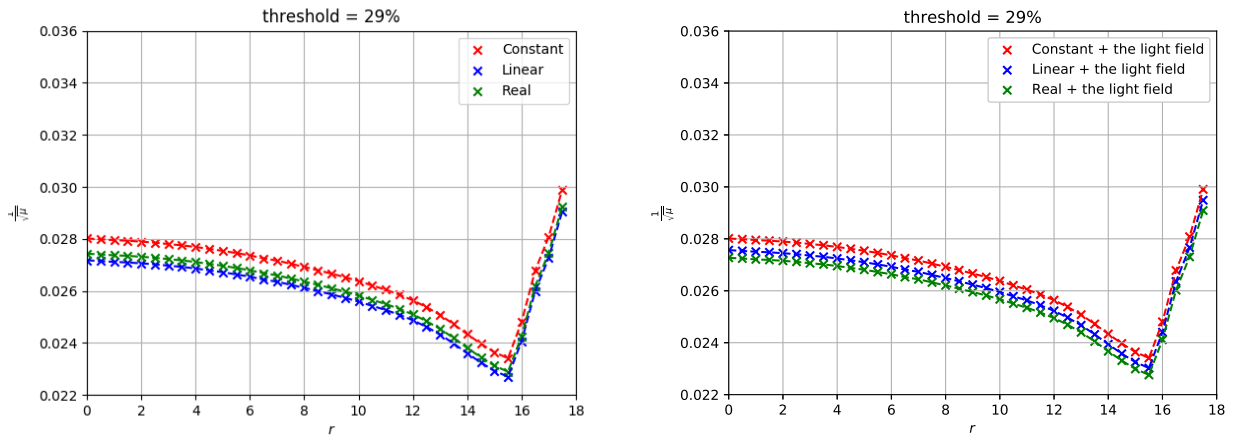


Figure 4.3: Detector energy resolution as a function of the distance from the center of detector to the event point with testing threshold $PDE_{th} = 29\%$.

Light field distribution in the container influence on the energy detector resolution for various models in different ways. To see this more obviously let's redraw previous figures in this chapter separately for all considered models adding also another thresholds (Figures 4.4 - 4.6).

As expected from the theory there is no difference for "constant" model as it doesn't matter what type of belt weights is used because they both give 1 in total (Figure 4.4).

For "linear" model the situation changes. Adding the light field distribution into the consideration worsen the detector energy resolution (Figure 4.5).

But for "real" model the light field distribution improves the detector energy resolution for all the distances from the center of detector to the event point (Figure 4.6).

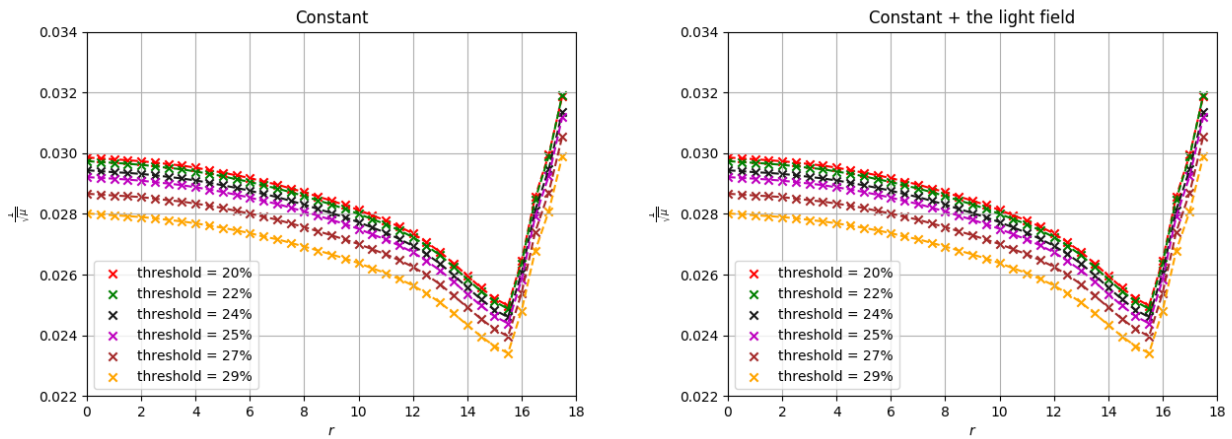


Figure 4.4: Detector energy resolution as a function of the distance from the center of detector to the event point for "constant" model.

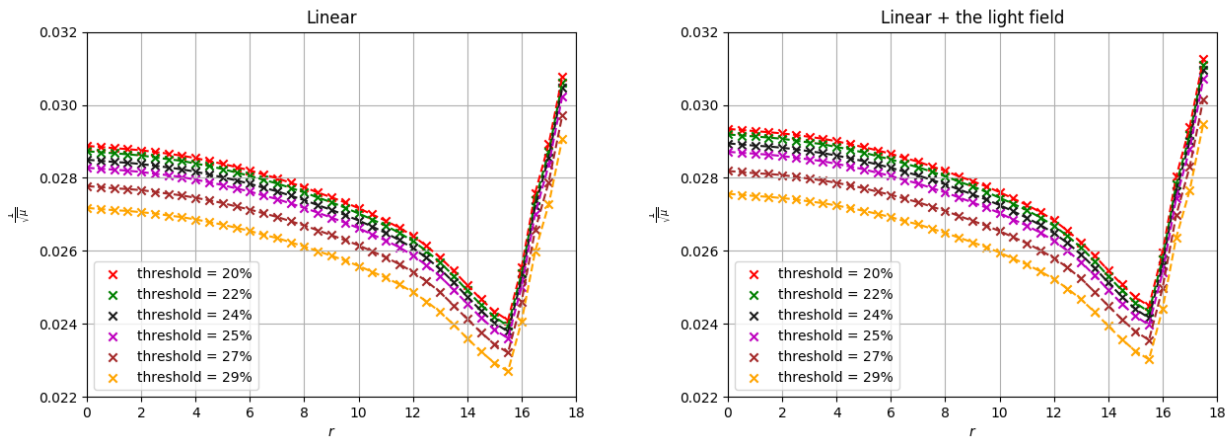


Figure 4.5: Detector energy resolution as a function of the distance from the center of detector to the event point for "linear" model.

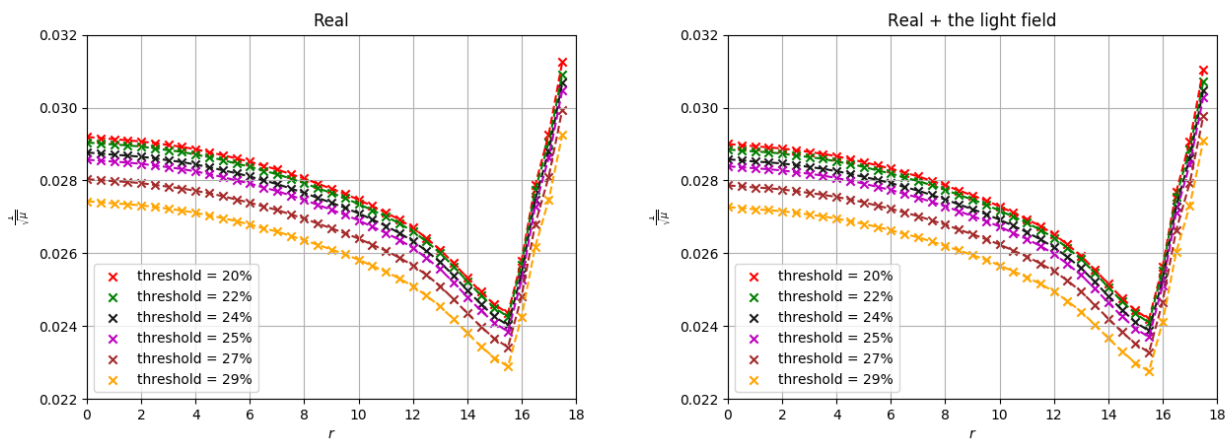


Figure 4.6: Detector energy resolution as a function of the distance from the center of detector to the event point for "real" model.

Knowing the mean number of photo-electrons gathered at each point μ we can calculate the χ^2 for three models with different thresholds (see Figure 4.7). The situation with the energy resolution repeats - adding of light field distribution in the belt weights worsen the χ^2 for "linear" model but improves it for "real" model (see Figure 4.8).

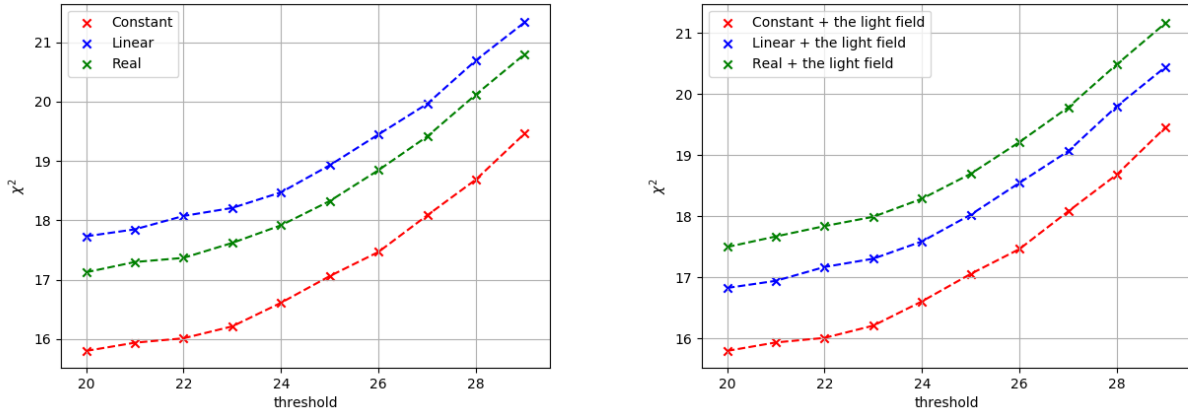


Figure 4.7: χ^2 as a function of PDE_{th} for different models.

The dependence of χ^2 from the threshold PDE_{th} isn't linear like it was if all PMTs had the same PDE distribution map. For larger threshold each χ^2 is bigger and bigger due to adding PMTs with greater \overline{PDE} into the detector. To obtain large χ^2 in the experiment we need to set up a quite big threshold for PMT testing process. The result χ^2 from nowadays threshold of 24% is good enough. Of course we can count on better results if the number of all testing PMTs can allow us to set up bigger threshold.

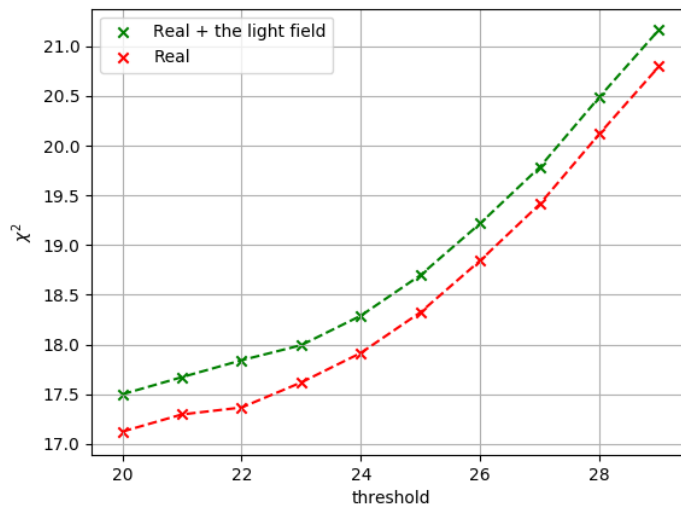


Figure 4.8: Influence of light field distribution in the container on the χ^2 as a function of PDE_{th} for "real" model.

Conclusion

During the summer student's practice, the following was done:

1. The simulation of optical processes inside the detector and PMT was made for three models ("Constant", "Linear" and "Real") and various thresholds. We used two different methods for belt weights calculation:
 - calculating the contribution of each zone of the belt to the entire PMT surface;
 - the same, but also taking into account the distribution of the light field inside the container.
2. It was found out that the light field distribution inside the container affects the detector energy resolution and χ^2 for these models in different ways. For "real" model which represents the PMTs in JUNO experiment in the most proper way this light field distribution is necessary to deal with because its consideration improves the energy resolution and χ^2 of JUNO experiment.

Bibliography

- [1] An F. Neutrino Physics with JUNO / F. An, G. An, Q. An, et al. // arXiv:1507.05613v2 [physics.ins-det]
- [2] Anfimov N. Large photocathode 20-inch PMT testing methods for the JUNO experiment / N. Anfimov // arXiv:1705.05012 [physics.ins-det]
- [3] Motta D. Optical properties of bialkali photocathodes/ D. Motta, S. Schonert/ /Nuclear Instruments and Methods in Physics Research A 539. - 2005.- P. 217–235.
- [4] The White book: JINR Neutrino Program / Eds. V. A. Bednyakov, D. V. Naumov. - Dubna: JINR, 2014. - 291 p., ill.
- [5] Кондрашов В.Е. Оптика фотокатодов / В.Е. Кондрашов - М.: Наука, 1976. - 208 с.